PLANETARY SCIENCE

Meteorite evidence for partial differentiation and protracted accretion of planetesimals

Clara Maurel[1]*, James F. J. Bryson[2], Richard J. Lyons[3], Matthew R. Ball[2], Rajesh V. Chopdekar[4], Andreas Scholl[4], Fred J. Ciesla[3], William F. Bottke[5], Benjamin P. Weiss[1]

Modern meteorite classification schemes assume that no single planetary body could be source of both un-melted (chondritic) and melted (achondritic) meteorites. This dichotomy is a natural outcome of formation models assuming that planetesimal accretion occurred nearly instantaneously. However, it has recently been pro-posed that the accretion of many planetesimals lasted over ≳1 million years (Ma). This could have resulted in partially differentiated internal structures, with individual bodies containing iron cores, achondritic silicate mantles, and chondritic crusts. This proposal can be tested by searching for a meteorite group containing evi-dence for these three layers. We combine synchrotron paleomagnetic analyses with thermal, impact, and colli-sional evolution models to show that the parent body of the enigmatic IIE iron meteorites was such a partially differentiated planetesimal. This implies that some chondrites and achondrites simultaneously coexisted on the same planetesimal, indicating that accretion was protracted and that apparently undifferentiated asteroids may contain melted interiors.

INTRODUCTION

Meteorites are divided into two principal groupings: chondrites, which are unmelted accretional aggregates, and achondrites, which are products of planetary melting processes (1). Among the achondrites, the existence of iron meteorites indicates that some planetesimals—the ~1- to 1000-km-diameter building blocks of the planets—underwent melting and large-scale differentiation to form a metallic core overlain by a silicate mantle. The existence of chondrites and achondrites has commonly been interpreted as evidence for a dichotomy in the planetesimal population: These bodies either never melted or other-wise melted throughout their entire interiors (2).

This apparent dichotomy has fundamentally shaped modern meteorite classification schemes, which are built upon the assump-tion of distinct spatial and temporal evolutions for meteorite parent bodies (1). Because the internal structures of planetesimals reflect the timing and mechanisms of their accretion due to early heating by the short-lived radionuclide ^{26}Al [half-life, 0.717 million years (Ma)] (3), this framework has been interpreted as evidence that chondritic parent bodies formed later than their achondritic counter-parts to have avoided melting (4). However, some modern accretion models predict that many planetesimals experienced an initial phase of rapid growth during the first ~1 to 2 Ma after the formation of calcium-aluminum–rich inclusions (CAIs), followed by the accu-mulation of residual chondritic material during the subsequent ≳1 Ma (5, 6). The resulting planetesimals are expected to be only partially melted and differentiated, leading to a continuum of differ-entiation end states including objects with metallic cores, melted achondritic silicate interiors, and unmelted chondritic crusts (7, 8).

Petrological, isotopic, and paleomagnetic studies have provided indirect evidence for the existence of bodies containing both melted and unmelted regions. For example, type 7 chondrites (e.g., the H7 chondrite Watson 012 or the C7 chondrite NWA 3133) have evi-dence of equilibrium-based silicate partial melting (9, 10). These meteorites could have originated from a transition region between subsolidus and melted silicates in partially differentiated parent bodies. Achondrite and chondrite groups sharing similar isotopic (particularly oxygen) and elemental compositions could also repre-sent different layers of partially differentiated parent bodies. This has been suggested for the IVA irons and L/LL chondrites, the un-grouped achondrite NWA 011 and CV chondrites, or the IIE irons and the H chondrites [as summarized in (8)]. Lastly, paleomagnetic records of dynamo-generated fields found in meteorites of the CV, L/LL, H, and R chondrite groups (11–15) have further favored the existence of chondritic layers covering planetesimals with differen-tiated interiors (Fig. 1).

Nonetheless, a longstanding challenge to the partial differentia-tion hypothesis has been the apparent absence of a meteorite group containing petrographic evidence for all the layers expected in a partially differentiated body (metallic core, melted mantle, and unmelted crust) (4). A possible exception is the IIE iron meteorite group. For more than 50 years, the IIE irons have defied simple clas-sification as chondrites or achondrites (16, 17). They are composed of an Fe-Ni matrix containing a diversity of both chondritic and achondritic silicate fragmental inclusions that experienced different levels of thermal metamorphism and degrees of differentiation (18). The similar oxygen isotopic compositions of both types of silicates nevertheless suggest that they originated on a single parent body (19). The textures of several achondritic silicates in different IIE irons indicate that they cooled near or below their solidus at >2.5°C hour^{-1} (text S1), suggesting that they were exposed to near-surface temperatures during a catastrophic event (18). However, these textures are difficult to reconcile with the idea of impact-induced melting of the silicates (text S2) (20). Together, these data have motivated the proposal that the IIE parent body was partially differentiated and that silicates from the melted mantle and the

[1]Department of Earth, Atmospheric, and Planetary Sciences, Massachusetts Institute of Technology, Cambridge, MA 02139, USA. [2]Department of Earth Sciences, University of Cambridge, Cambridge CB2 1TN, UK. [3]Department of the Geophysical Sciences, The University of Chicago, Chicago, IL 60637, USA. [4]Advanced Light Source, Lawrence Berkeley National Laboratory, Berkeley, CA 94720, USA. [5]Southwest Research Institute and NASA Solar System Exploration Research Virtual Institute–Institute for the Science of Exploration Targets, Boulder, CO 80302, USA.
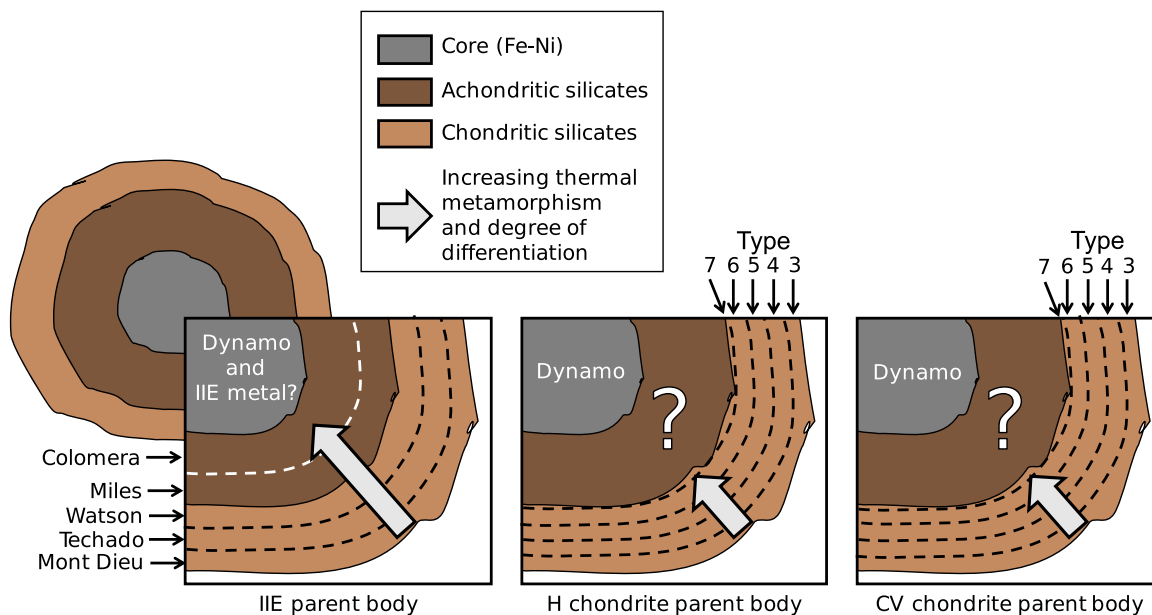*Corresponding author. Email: cmaurel@mit.edu

Fig. 1. IIE meteorites contain evidence for all the expected layers of a partially differentiated body. Diagrams illustrate how IIE meteorites contain both chondritic and achondritic silicate inclusions exhibiting different degrees of metamorphism/differentiation depending on the meteorite. Mont Dieu is one of the least heated and contains chondrules. Techado and Watson show more evidence of thermal alteration. In addition, some IIE irons contain achondritic silicates, exhibiting different degrees of differentiation ranging from Miles with pyroxene-enriched basaltic silicates to Colomera with silicates of andesitic composition (56, 57). This study provides the missing evidence that the IIE parent body had a metallic core. Direct petrologic evidence for achondritic materials on the CV and H chondrite parent bodies remains to be confirmed.

unmelted crust were mixed with endogenous or exogenous metal during an impact (18).

However, this scenario has yet to be widely accepted because it is missing two key pieces of supporting evidence. First, there has been no compelling evidence that the IIE parent body had a metallic core. For example, the siderophile element compositions of IIE irons do not exhibit fractionation trends expected for a core undergoing fractional crystallization (text S2) (20). Second, it has yet to be demonstrated that an impact could have form a mixed metal-silicate reservoir in a parent body without catastrophically disrupting the body. Here, we use paleomagnetic analyses to search for the existence of a molten metallic core within the IIE parent body. We are motivated by the fact that if the IIE parent body had a metallic core, it could have powered a dynamo-generated magnetic field that would imprint a natural remanent magnetization (NRM) in the IIE meteorites (21). We then combine these paleomagnetic measurements with impact simulations, thermal modeling, and collisional evolution considerations to establish the likelihood that impacts could form IIE-like iron meteorites.

RESULTS

Paleomagnetic experiments

We selected the IIE iron meteorites Colomera and Techado, which contain achondritic and chondritic silicate inclusions, respectively (18). Their metal matrices contain cloudy zones (CZs), nanoscale intergrowths of ferromagnetic Ni-rich islands embedded in a paramagnetic Ni-poor matrix (22) that form at kamacite-taenite (K-T) interfaces (fig. S1) during cooling at $\lesssim 10^{4\text{o}}C \ Ma^{-1}$ through ~350°C (23). Below 320°C, the crystal structure of CZ islands can order to form the ferromagnetic mineral tetrataenite (γ''-FeNi). Micromagnetic simulations indicate that during this transformation, a new

NRM independent of that of the precursor taenite is recorded (24). CZ islands can retain this NRM as a record of the ambient magnetic field present during tetrataenite formation over the history of the solar system (25).

We analyzed four K-T interfaces in Colomera and two in Techado (Fig. 2). We used the synchrotron-based technique x-ray photo-emission electron microscopy (XPEEM) to image the x-ray magnetic circular dichroism (XMCD) signal of multiple locations along each of the interfaces (26). This technique enables isolation of the vector NRM carried by the CZ from that of the large surrounding kamacite and taenite grains, which are poor magnetic recorders. Although individual CZ islands (~10 to 150 nm in size) are not resolved, we can estimate the bulk NRM of micrometer-sized regions of the CZ by comparing the XMCD data to that expected for an underlying Maxwell-Boltzmann distribution of the islands' magnetization directions (Fig. 3; see Materials and Methods and text S3) (14).

We obtained paleodirections from CZ islands located in a 0.5- to 2-μm-wide region of interest next to the tetrataenite rim (Fig. 4, fig. S1, and text S3). Each K-T interface was then analyzed using electron backscattered diffraction to mutually orient their NRM directions (text S4). We found that we cannot reject at 95% confidence the hypothesis that all of the CZs within each meteorite share a common mean paleodirection (text S5). This result excludes spontaneous magnetization acquired in zero-field environment as a source of the observed signal and indicates that the meteorites both cooled in the presence of a substantial field.

The analytical method based on Maxwell-Boltzmann statistics also provides paleointensity estimates. We estimated that Techado and Colomera experienced ancient field intensities of 36 ± 11 μT and 15 ± 5 μT, respectively (text S3). These uncertainties are 2 SE accounting for the measurement noise, the limited number of islands included in each dataset, and the island size distribution at the tetrataenite-formation
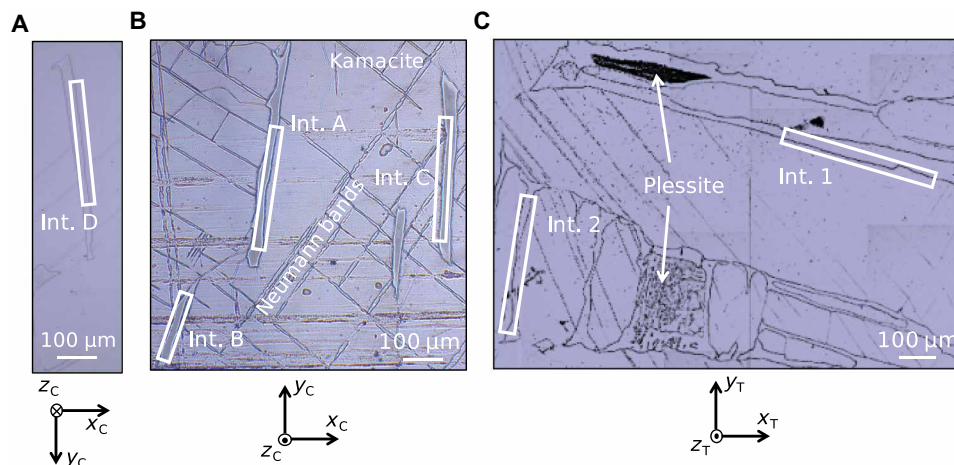
Fig. 2. Reflected light images of the four K-T interfaces analyzed in Colomera and Techado. (A) K-T interface D in Colomera. Interface D is located on the other side of the sample with respect to A, B, and C ~5 mm away from K-T interface C; the reference frame indicates how the sample is rotated with respect to (B). The subscript "C" of the reference frame refers to "Colomera." (**B**) K-T interfaces A, B, and C in Colomera. The CZs are clearly recognizable by their dark gray color, with the surrounding light gray tetrataenite rim and embedded in the kamacite medium gray matrix. Neumann bands (shock-induced twinning of the kamacite crystal) are shown. The subscript C of the reference frame refers to Colomera. (**C**) K-T interfaces 1 and 2 in Techado. Plessite is visible. The subscript "T" of the reference frame refers to "Techado." The two meteorite samples (Colomera and Techado) are not mutually oriented. For each image, the sample had been polished and etched between 15 and 25 s with nital (98% ethanol, 2% nitric acid).
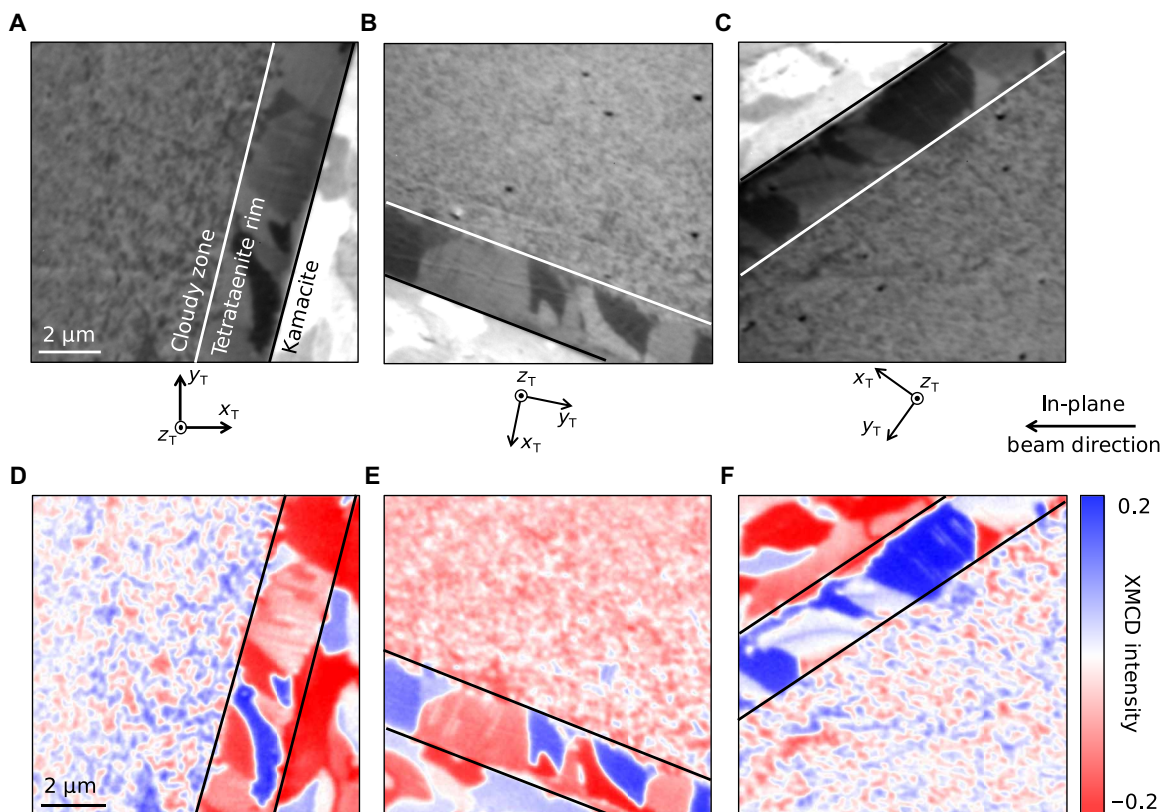

Fig. 3. Measuring the three components of NRM using XPEEM. (A to **C)** Single-polarization XPEEM images of one region of K-T interface 2 in Techado taken at three different orientations of the sample with respect to the x-ray beam. The gray scale quantifies the flux of electron captured in the optics. The beam hits the sample at 30° with respect to the plane of the image (its in-plane direction is shown with an arrow). The reference frame refers to Fig. 2. (**D** to **F**) Corresponding XMCD images obtained when combining the corrected XPEEM images obtained with left- and right-circular polarizations.
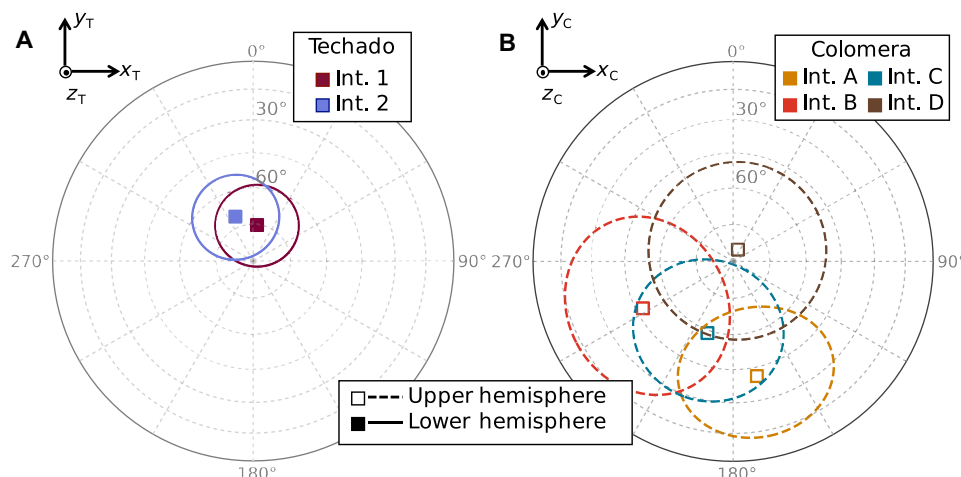
Fig. 4. Ancient field directions recovered from each K-T interface in Techado and Colomera. (**A**) Average paleofield directions estimated from the two K-T interfaces in Techado (1 and 2). (**B**) Average paleofield directions estimated from the four K-T interfaces in Colomera (A to D). Shown in (A) and (B) are equal area projection in the reference frames of Fig. 2. Open (closed) symbols and dashed (solid) lines denote upper (lower) hemisphere. Ellipses represent the 95% confidence interval accounting for the measurement uncertainty, the small-number statistical uncertainty, and the uncertainty associated with the mutual orientations of the CZs.

temperature (text S6). Although they confidently exclude zero field conditions, they do not account either for systematic uncertainties associated with magnetostatic interactions between islands or for an induced field component from the dominant kamacite in the IIE reservoir. The former could result in an intensity underestimated by up to an order of magnitude (27); the latter could yield paleointensities overestimated by a factor of up to ~3 assuming a spheroidal metal reservoir (text S7). Therefore, the full ranges of paleointensity estimated for Techado and Colomera are 10 to 360 µT and 5 to 150 µT, respectively.

Origin of the magnetization
The meteorites acquired their NRM when they cooled through the tetrataenite formation temperature (320°C). Using a thermodynamical model of CZ formation (28), we found that Techado and Colomera cooled through ~350°C at 4.6 ± 1.9°C Ma^{-1} and 2.5 ± 1.4°C Ma^{-1}, respectively. This is consistent with the slow cooling ($\lesssim$5000°C Ma^{-1}) required for subsequent tetrataenite formation at 320°C due to the very slow atomic diffusion of Ni at this temperature (texts S8 and S9) (29). For such cooling rates (i.e., of the order of ~10°C Ma^{-1}), the tetrataenite formation temperature is within error of the estimated Ar closure temperature of 330 ± 70°C (2 SD) for 0.1- to 1-mm size feldspars, the dominant ^{40}Ar-bearing minerals in both meteorites (text S1) (30, 31). Therefore, the measured ^{40}Ar/^{39}Ar ages indicate that Techado and Colomera recorded a magnetic field of approximately 78 ± 13 Ma and 97 ± 10 Ma after the formation of CAIs, respectively (31). A subsequent short-lived thermal event like brief impact heating (e.g., 600°C for a minute) that would reset the NRM but not disturb the ^{40}Ar/^{39}Ar ages is excluded by the fact that such events would remove CZ and tetrataenite (32).

The magnetizing field could conceivably have been generated by at least four main sources: the solar nebula, the early solar wind, impacts, or a core dynamo. The relatively young age of the NRM rules out the solar nebula, which dissipated within 5 Ma after CAI formation (33). On the other hand, the slow kinetics of tetrataenite formation exclude time-variable or transient field sources like the

early solar wind and impact-generated plasma, which are expected to have varied on time scales shorter than a few days (34, 35).

This leaves one remaining source capable of magnetizing Colomera and Techado: a core dynamo. Because core dynamos powered by thermal convection were only sustainable during <20 Ma after planetesimal formation (36, 37), the dynamo would have been powered by the thermochemical convection driven by core crystallization. Such a dynamo could feasibly have initiated within a few tens of million years following planetesimal formation and been sustained until the core fully solidified (37). Assuming a planetocentric dipolar geometry, dynamos powered by thermal convection can produce field intensities 0.002 to 60 µT midway through the silicate layer of a planetesimal with core radius equal to 33% of its total radius (text S10) (21). Dynamos powered by core crystallization may generate more intense fields than those powered by thermal convection (38), which is consistent with our estimated paleointensities. We conclude that Techado and Colomera were most likely magnetized by such field, which, in turn, requires that the IIE planetesimal had a metallic core.

Thermal evolution and high-velocity impact simulations
Our results place important constraints on the IIE parent body. If the meteorites formed through an impact, the core must have been preserved and at most be partially crystallized at least until Colomera's ^{40}Ar/^{39}Ar age (~97 Ma after CAI formation). Moreover, to explain the formation of CZs, this impact must have emplaced the IIE metal-silicate mixture at a depth where it could cool sufficiently slowly. In the following, we test the compatibility of these constraints with impact-induced formation on a partially differentiated body. Our simulations act as a proof of concept; they are not meant to identify the specific set of impact conditions that could form an IIE reservoir.

We first address the issue of whether a core could only be partially crystallized when the IIE irons acquired their NRM. We simulated the convective and conductive cooling of partially differentiated planetesimals using a simple, one-dimensional (1D) model where planetesimals form in two instantaneous accretion events (Materials and Methods; fig. S6A). For partially differentiated bodies

of radius >170 km with a core radius >50 km, we found that the core fully crystallizes later than the estimated acquisition times for the meteorites' NRM (fig. S6B). On such planetesimals, a IIE reservoir buried between ~30 and ~60 km below the surface is compatible with Techado's and Colomera's $^{40}Ar/^{39}Ar$ closure temperature-age and cooling rate constraints (Fig. 5).

This still leaves open the question of whether an impact on a 170-km radius body could create a IIE reservoir in the upper part of its silicate layer while preserving a core. We addressed this by conducting a suite of 2D impact simulations using the iSALE2D (impact-simplified arbitrary Lagrangian Eulerian 2D) shock hydrodynamics code (39). We focused on two idealized scenarios involving either a pure chondritic or pure iron impactors impacting at 30 Ma after CAI formation, where ~20% of the target's silicate layer is still above its solidus (~1100°C; Fig. 6A). We simulated >10-km radius impactors with velocities <9 km s^{-1} (text S12). These objects are likely larger and slower than the population dominating the early solar system (40). However, by analogy to scaling laws applied to crater formation, we estimate that smaller impactors and higher impact velocities would yield similar outcomes (text S13).

We find that impacts between 4 and 5 km s^{-1} by a purely chondritic object can result in portions of the target's molten core being sequestered into the silicate layer and subsequently impeded from percolating back to the stirred-up core (Fig. 6B). On the other hand, a pure iron impactor can be implanted permanently in the upper half of the silicate layer at low impact velocity (1 km s^{-1}; Fig. 6C). In both cases, the liquid or solid metal equilibrates to the temperature of its surroundings by conduction and the planetesimal is left with potential IIE-like metal-silicate reservoirs compatible with IIE siderophile element patterns showing no obvious fractional crystallization trend (20).

DISCUSSION

Like nearly all asteroidal meteorites, IIE irons are inferred to have originated from a parent body presently located in the asteroid belt (although this could be a fragment of a larger body that was catastrophically disrupted). Two scenarios can be considered to explain where and how likely a planetesimal could have been impacted to form the IIE meteorites. It is possible that (i) the IIE parent body was already in the asteroid belt at the time of the impact or (ii) the IIE parent body was impacted in the terrestrial planet region [≲2 astronomical units (AU)] and was then dynamically captured into the main belt. According to collisional evolution models (text S14), scenario 1 appears improbable. It would require a number of potential 10-km radii impactors equivalent to 200 times the current population of the main asteroid belt to exist on crossing orbits with the IIE parent body >30 Ma after CAI formation (41).

Moving the IIE-forming impact to the terrestrial planet region, as described in scenario 2, would increase the collision probabilities for impactors to strike the IIE parent body and thereby reduce the number of projectiles needed to get a very large impact at >30 Ma after CAIs. These conditions may have been readily achievable during the late stages of terrestrial planet formation, when collisions between protoplanets, or the giant impact that made the Moon, were potentially liberating large quantities of iron-rich debris [e.g., (42)]. The size distribution of these fragments is unknown. However, simply based on the volume ratio between the mantle of a planetary embryo and its core for a body of chondritic bulk composition, the volume ratio between metal-rich and silicate fragments would only be <10% (43). This suggests that more than one giant impact might be needed to obtain an acceptable population of potential iron-rich impactors and decreases the plausibility of such scenario.

Could the IIE parent body have been transported from the inner solar system to the main asteroid belt after an impact at 30 Ma after CAI formation? A recent numerical model suggests that during terrestrial planet formation, gravitational scattering efficiently transported planetesimals from the inner solar system to the current main asteroid belt (44). According to the simulations, half the initial population of planetesimals would have been implanted in the main belt by ~60 Ma after CAI formation, allowing the IIE-forming impact to occur in the inner solar system region. The increase in eccentricity necessary for belt-crossing trajectories could also have favored impacts among planetesimal and embryo fragments.

From a dynamical capture perspective, planetesimals that formed in the 1.5 to 2 AU region are more likely to have intact or fragmented
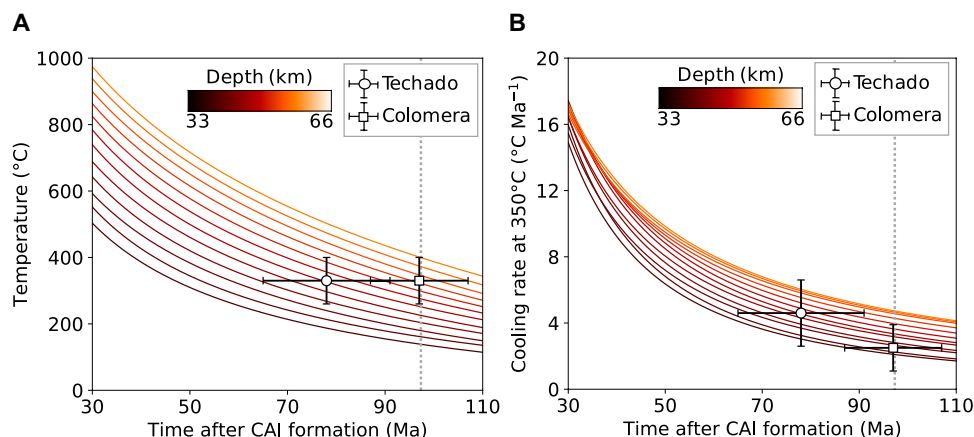

Fig. 5. Cooling profiles of a partially differentiated IIE parent body. (A) Time-temperature constraints. Circle and square denote $^{40}Ar/^{39}Ar$ ages for 0.1- to 1-mm feldspar grains for Techado and Colomera, respectively (30). Curves represent the temperature of material on a 170-km radius, partially differentiated planetesimal at depths between 33 and 66 km below the surface. (B) Time-cooling rate constraints on same body shown in (A). Circle and square denote cooling rates at ~350°C of Techado and Colomera, respectively. Curves show the evolution of the cooling rate at same depths as in (A). In (A) and (B), the dotted line shows when the core of the planetesimal is completely crystallized and error bars indicate 2 SD.
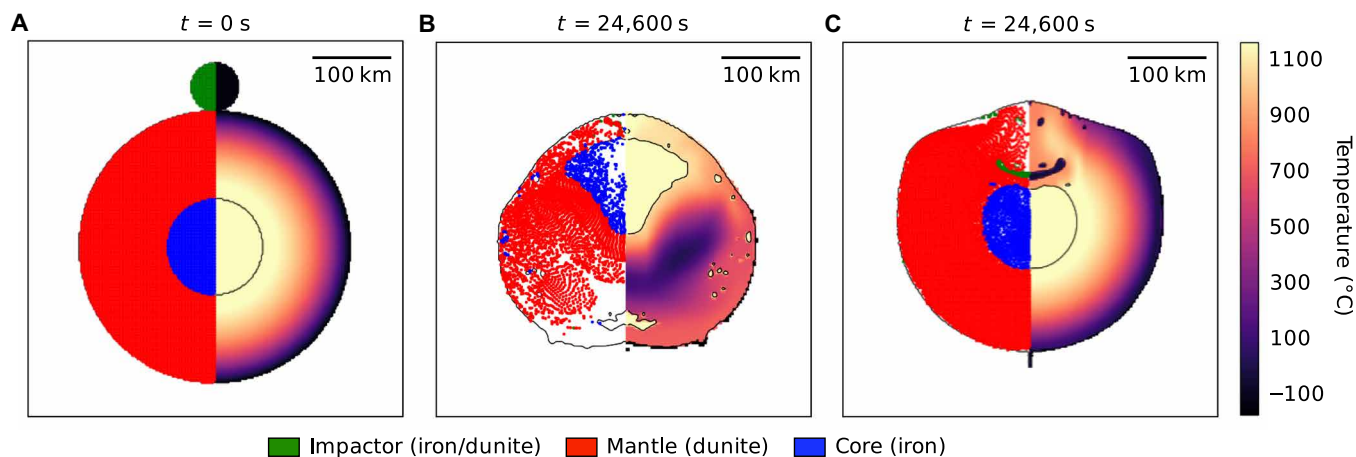
Fig. 6. Initial and final states of representative IIE-forming, 2D impact simulations. (**A**) Initial state of a 170-km radius target with a 60-km radius iron core and a 110-km-thick dunite layer before impact. Impactor is 30 km in radius, is solid, and is made of either iron or dunite. The left half of the figure shows the constituent materials, and the right half shows the temperature obtained from the thermal evolution model at 30 Ma after CAI formation. (**B**) End of the impact simulation after 24,600 s for a 40-km radius, dunite impactor impacting vertically at 5 km s^{-1}. Small amounts of core material are placed in the upper half of the target's silicate layer. A finite number of tracers were used to identify the different materials on the left half of the figure; this can result in regions with no tracers (white) but does not mean that no material is present at these locations. (**C**) End of the impact simulation (after 24,600 s) for a 30-km-radius iron impactor impacting vertically at 1 km s^{-1}.

remnants in the current main asteroid belt than planetesimals formed closer to the Sun. It is possible that (*4*) Vesta was one of them (*45*). The existing five apparently metal-rich asteroids >50-km radius (*46*) could be relics of differentiated planetesimals formed in the terrestrial planet region; these bodies also have sizes comparable to the largest metallic impactors assumed in our simulations. The NASA Discovery mission Psyche, which plans to visit the largest M-type asteroid (*16*) Psyche in 2026, will shed light on the plausible link between metal-rich asteroids and the core of ancient planetesimals (*47*).

Our findings show that the IIE irons most likely formed from impact mixing of materials that originated on a single planetesimal exhibiting the full range of planetary differentiation states: metallic core, melted silicate mantle, and unmelted silicate crust. The silicates in the IIE irons likely formed on the same body, while the iron matrix could have originated from the same body as the silicates or else from a metallic impactor. Combined with earlier studies indicating partial differentiation of the CV, H, L/LL, and R chondrite parent bodies, this indicates that partial differentiation was likely a common end state for planetesimals (*7*, *9–15*). It has even been suggested that H chondrites themselves could have originated on the IIE parent body (*8*). This, in turn, supports a two-stage formation process involving early initial accretion and differentiation followed by later protracted accretion of a chondritic, undifferentiated crust, as proposed by most recent accretion models (*5*, *6*). A consequence is that some chondrite and achondrite meteorite groups likely coexisted on the same planetesimal, challenging the topology of existing meteorite classification schemes.

MATERIALS AND METHODS
Paleomagnetic experiments
Figure S1 graphically summarizes the various geometric quantities associated with our XPEEM measurements. The XPEEM experiments were conducted at the beamline 11.0.1.1 of the Advanced Light Source (ALS) at the Lawrence Berkeley Laboratory. Polished samples were first argon-sputtered with the following sequence: 8 hours at a voltage

of 1.2 keV and 4 mA intensity, 6 hours at 0.8 keV and 4 mA, and 1 hour at 0.6 keV and 4 mA. This sequence typically sputters a thickness of ~80 nm of material from the surface, removing any oxidation that occurred during polishing. XPEEM images were acquired with a 10-μm field of view along each CZ (fig. S3). At each location, two images (left- and right-circular polarization) were acquired with the x-ray beam tuned at the Fe L$_3$ absorption edge (707.4 eV) along with two others, with the beam tuned off-edge (702 eV) to capture the background signal (i.e., the constant flux of secondary electrons generated by the excitation of atoms other than Fe). Each of these four left- and right-circular polarization images was taken sequentially five times, and the whole sequence of 20 images was itself repeated four times to minimize the effect of possible x-ray beam drifts during the measurements and to reduce noise. Once XPEEM images were acquired for all K-T interfaces of interest in one sample orientation, the sample was rotated by approximately 120° with respect to the initial orientation along an axis normal to the sample surface and each location was measured again using the same imaging sequence. Once all the locations had been imaged in this second orientation, we rotated the sample another 120° and repeated the same procedure for this third orientation (Fig. 3). In total, for Colomera, we analyzed an 80-μm-long transect along K-T interface A (8 locations), a 70-μm-long transect along interface B (7 locations), a 100-μm-long transect along interface C (10 locations), and a 130-μm-long transect along interface D (13 locations), while for Techado we analyzed a 250-μm-long transect along K-T interface 1 (25 locations) and a 330-μm-long transect along interface 2 (33 locations; Fig. 2). In total, this produced a minimum of 560 and a maximum of 2640 left- and right-polarization images (for interface B and interface 2, respectively).

Our experimental protocol and approach to data processing builds upon that described in (*14*). The amount of absorbed circularly polarized x-rays depends on the angle between the helicity of the x-ray and the local magnetization direction, as well as contributions from the sample work function, elemental concentration of iron, and oxidation state of the element of interest. The contrast between

XPEEM images obtained with left- and right-circularly polarized x-rays, called XMCD, is proportional to the local sample magnetization direction and magnitude (*48*). To obtain XMCD contrast maps, we first subtracted the average images obtained for both x-ray polarizations at on-edge (707.4 eV) and off-edge energies (702 eV) to remove the contribution to the XPEEM signal from atoms other than Fe. To compensate for gradual fluctuations in the incoming x-ray flux and improve the XMCD contrast, we also divided the pixel intensities by their off-edge values

$$I_{corr}^{\pm} = \frac{I_{on-edge}^{\pm} - I_{off-edge}^{\pm}}{I_{off\,edge}^{\pm}} \qquad (1)$$

This correction with off-edge images was only applied systematically for Techado because not all K-T interfaces of Colomera (measurement campaigns pre-dating that of Techado) were analyzed off-edge. The correction applied for these images is described in text S3.

XMCD contrast maps (Fig. 3) were generated for each location along each CZ by combining the corrected XPEEM images as follows

$$I_{XMCD} = \frac{I_{corr}^{-} - I_{corr}^{+}}{I_{corr}^{-} + I_{corr}^{+}} \qquad (2)$$

where I_{XMCD} is a pixel intensity on the XMCD contrast map, and I_{corr}^{-} and I_{corr}^{+} are the intensities of the same pixel on a corrected XPEEM image obtained with right and left circularly polarized x-rays, respectively. On these XMCD contrast maps, three shades of red and three shades of blue are observable in the tetrataenite rim, which correspond to spatially resolved, micrometer-sized magnetic domains formed from the same parent taenite as the CZ. For each XMCD image, we recorded the I_{XMCD} values of these six colors, which correspond to the six preferred orientations of the magnetization of tetrataenite (the <100> crystallographic axes of the parent taenite). Because of the islands' small sizes (between 102 and 125 nm, on average, for the largest islands in Techado and Colomera, respectively; text S8), the XMCD contrast of individual CZ islands cannot be resolved; instead, a continuum of red and blue colors is visible in the CZ. The average intensity of a 0.5-μm-wide region of interest was collected for each XMCD images of Techado. We used a 2-μm-wide region for Colomera (text S3). These quantities are used to calculate the three spatial components of the ambient field that magnetized the meteorite by comparing the XMCD data to that expected for a Maxwell-Boltzmann distribution of their magnetization directions. The theoretical approach is described in detail in text S3.

Thermal modeling
A full description of the model and all of the parameter values are presented in (*37*). Here, we provide a summary of the procedure. We adopted a model in which the growth of the body to its final radius occurs in two discrete steps. The first instantaneous accretion event occurs sufficiently early that the accreted material contains abundant ^{26}Al (*3*), which causes this material to heat up to its partial melting temperature and differentiate into a core and partially molten magma ocean within less than 0.25 Ma after accretion. The second accretion event occurs at a later time such that the material added during this event contains substantially less ^{26}Al and does not heat up to its partial melting temperature through radiogenic heating. Hence, this second accretion event results in the addition of an un-

melted, chondritic crust to the surface, forming a partially differentiated planetesimal. This is analogous to the two phases of accretion that are observed in accretion models incorporating detailed dynamics (*6*).

All the simulations that we conducted had their first accretion event occur at 0.5 Ma after CAI formation. The precise timing of this accretion event has a minor effect on the resulting planetesimal as long as it occurs when the decay rate of ^{26}Al is sufficient to melt the planetesimal seed (≲1.8 Ma after CAI formation) (*37*). The second accretion event occurs in all the simulations at 2.4 Ma after CAI formation. This time was chosen because at this point, the remaining ^{26}Al in the added material produces a temperature in the unmelted crust up to the peak metamorphic temperature estimated for Netschaëvo (~900°C), another IIE with chondritic silicate inclusions (*49*). We use this temperature as an estimate for Techado in the absence of a published value for this meteorite. We simulated the thermal evolution of bodies with initial radii (after the first accretion event) of 100, 130, 180, and 230 km. The radii of all of these bodies increased instantaneously by 70 km during the second accretion event, creating bodies with final radii of 170, 200, 250, and 300 km, respectively (fig. S6). Simulating a linear, protracted accretion of the 70-km-thick chondritic crust between 0.5 and 2.4 Ma after CAI formation would result in an average accretion rate of ~35 km Ma^{-1}. This is two orders of magnitude faster than heat dissipation by conduction through the deposited chondritic material, equal to ~0.3 km Ma^{-1} assuming a thermal diffusivity of ~9×10^{-7} m^{2} s^{-1}. Therefore, simulating instantaneous accretion of the crust actually results in comparable amounts of crustal material being melted at the contact point with the seed as would have occurred for constant accretion. It produces in a similar structure of the planetesimal at the end of accretion.

Regardless of the uncertainties surrounding the mechanism that could drive compositional dynamos, a core cannot generate a magnetic field once it is completely solid. As a consequence, we considered that a crystallization-driven dynamo could have been generated during the time window before the latent heat resulting from solidification of the entire core at the Fe-S eutectic temperature (930°C) was extracted across the core-mantle boundary (i.e., while the core is at least partially molten). Our 170-km final radius simulation has core solidification finishing at 97 Ma after CAI formation (the approximate age of NRM acquisition by the CZs in Colomera), suggesting that it is unlikely that bodies with radii smaller this value were able to exhibit dynamo activity when Colomera recorded its remanence. It is therefore possible that both Techado and Colomera could have been magnetized by compositionally driven activity if the final radius of their parent body was ≥170 km (fig. S10). It should also be noted that the core must have started to crystallize before Techado acquired its magnetization 78 ± 13 Ma after CAI formation. This timing is compatible with Re-Os ages estimated for the IIABs [37 ± 50 Ma after CAI formation (*50*)], which are often taken as an example of a fractionally crystallized group that originated in an undisturbed mantled core.

High-velocity impact simulations
The numerical simulations were conducted using the latest version of the iSALE2D shock hydrodynamics code (*39*, *51*, *52*), iSALE-Dellen, with a cylindrically symmetric computational mesh (*53*). Given the 2D geometry of the simulations, only vertical impacts were simulated. The target planetesimal was 170 km in radius with a 60-km radius iron core and a 110-km-thick silicate layer. For simplicity, the same

material (dunite) was used to represent the material properties for the partially solidified mantle and never-melted crust. The initial thermal profiles of the target at 10 and 30 Ma after CAI formation were obtained from our 1D thermal model. These times are in agreement with a recent Hf-W isotopic investigation that dates the IIE-forming impact event(s) within the first tens of million years after CAI formation (54).

In all simulations, the core was molten ($T > 1250$ K) and treated as a fluid with a constant viscosity of 100 Pa s. For an impact at 10 Ma after CAI formation, 53% of the silicate layer is still above its solidus (~1100°C) and therefore is only partially molten. At 30 Ma, 27% of the silicate layer is above its solidus. We adopted the semi-analytical ANEOS package to determine the equation of state of each material using published rheological properties of dunite for the silicate layer and iron for the core (55). The spatial resolution was between 14 and 16 cells per projectile radius (CPPR), which resulted in a grid spacing between 2 and 2.5 km. The simulations were stopped after internal flows within the body had ceased. Depending on the scenario investigated, the projectile was entirely made of iron or dunite. In either case, the impactor had a radius ranging from 10 to 40 km and a velocity between 1 and 9 km s^{-1}. Table S6 summarizes the combinations of parameters investigated. Text S12 discusses additional simulations.

SUPPLEMENTARY MATERIALS

Supplementary material for this article is available at http://advances.sciencemag.org/cgi/content/full/6/30/eaba1303/DC1

REFERENCES AND NOTES

1. A. N. Krot, K. Keil, E. R. D. Scott, C. A. Goodrich, M. K. Weisberg, Classification of meteorites and their genetic relationships, in *Treatise on Geochemistry*, H. D. Holland, K. K. Turekian, Eds. (Elsevier, 2014), vol. 1, pp. 1–63.
2. B. Mason, Meteorites. *Am. Sci.* **55**, 429–455 (1967).
3. P. J. Hevey, I. S. Sanders, A model for planetesimal meltdown by ^{26}Al and its implications for meteorite parent bodies. *Meteorit. Planet. Sci.* **41**, 95–106 (2006).
4. E. R. D. Scott, Meteoritical and dynamical constraints on the growth mechanisms and formation times of asteroids and Jupiter. *Icarus* **185**, 72–82 (2006).
5. A. Johansen, M.-M. Mac Low, P. Lacerda, M. Bizzarro, Growth of asteroids, planetary embryos, and Kuiper belt objects by chondrule accretion. *Sci. Adv.* **1**, e1500109 (2015).
6. S. J. Weidenschilling, Accretion of the asteroids: Implications for their thermal evolution. *Meteorit. Planet. Sci.* **54**, 1115–1132 (2019).
7. L. T. Elkins-Tanton, B. P. Weiss, M. T. Zuber, Chondrites as samples of differentiated planetesimals. *Earth Planet. Sci. Lett.* **305**, 1–10 (2011).
8. B. P. Weiss, L. T. Elkins-Tanton, Differentiated planetesimals and the parent bodies of chondrites. *Annu. Rev. Earth Planet. Sci.* **41**, 529–560 (2013).
9. A. J. Irving, T. E. Larson, F. J. Longstaffe, D. Rumble, T. E. Bunch, J. H. Wittke, S. M. Kuehner, A primitive achondrite with oxygen isotopic affinities to CV chondrites: Implications for differentiation and size of the CV parent body, paper presented at the 85th American Geophysical Union Fall Meeting, San Francisco, CA, 2004.
10. A. W. Tait, A. G. Tomkins, B. M. Godel, S. A. Wilson, P. Hasalova, Investigation of the H7 ordinary chondrite, Watson 012: Implications for recognition and classification of Type 7 meteorites. *Geochim. Cosmochim. Acta* **134**, 175–196 (2014).
11. L. Carporzen, B. P. Weiss, L. T. Elkins-Tanton, D. L. Shuster, D. Ebel, J. Gattacceca, Magnetic evidence for a partially differentiated carbonaceous chondrite parent body. *Proc. Natl. Acad. Sci. U.S.A.* **108**, 6386–6389 (2011).
12. J. Gattacceca, B. P. Weiss, M. Gounelle, New constraints on the magnetic history of the CV parent body and the solar nebula from the Kaba meteorite. *Earth Planet. Sci. Lett.* **455**, 166–175 (2016).
13. J. Shah, H. C. Bates, A. R. Muxworthy, D. C. Hezel, S. S. Russell, M. J. Genge, Long-lived magnetism on chondrite parent bodies. *Earth Planet. Sci. Lett.* **475**, 106–118 (2017).
14. J. F. J. Bryson, B. P. Weiss, B. Getzin, J. N. H. Abrahams, F. Nimmo, A. Scholl, Paleomagnetic evidence for a partially differentiated ordinary chondrite parent asteroid. *J. Geophys. Res. Planets* **129**, 1880–1898 (2019).
15. C. Cournède, J. Gattacceca, P. Rochette, D. L. Shuster, Paleomagnetism of Rumuruti chondrites suggests a partially differentiated parent body. *Earth Planet. Sci. Lett.* **533**, 116042 (2020).
16. T. E. Bunch, E. Olsen, Potassium feldspar in Weekeroo Station, Kodaikanal, and Colomera iron meteorites. *Science* **160**, 1223–1225 (1968).
17. G. J. Wasserburg, H. G. Sanz, A. E. Bence, Potassium-feldspar phenocrysts in the surface of Colomera, and iron meteorite. *Science* **161**, 684–687 (1968).
18. A. Ruzicka, Silicate-bearing iron meteorites and their implications for the evolution of asteroidal parent bodies. *Geochemistry* **74**, 3–48 (2014).
19. K. H. McDermott, R. C. Greenwood, E. R. D. Scott, I. A. Franchi, M. Anand, Oxygen isotope and petrological study of silicate inclusions in IIE iron meteorites and their relationship with H chondrites. *Geochim. Cosmochim. Acta* **173**, 97–113 (2016).
20. J. T. Wasson, Formation of non-magmatic iron-meteorite group IIE. *Geochim. Cosmochim. Acta* **197**, 396–416 (2017).
21. B. P. Weiss, J. Gattacceca, S. Stanley, P. Rochette, U. R. Christensen, Paleomagnetic records of meteorites and early planetesimal differentiation. *Space Sci. Rev.* **152**, 341–390 (2010).
22. R. Blukis, R. Rüffer, A. I. Chumakov, R. J. Harrison, A high spatial resolution synchrotron Mössbauer study of the Tazewell IIICD and Esquel pallasite meteorites. *Meteorit. Planet. Sci.* **52**, 925–936 (2017).
23. C. W. Yang, D. A. Williams, J. I. Goldstein, A revision of the Fe-Ni phase diagram at low temperatures (< 400°C). *J. Phase Equilib.* **17**, 522–531 (1996).
24. J. F. Einsle, A. S. Eggeman, B. H. Martineau, Z. Saghi, S. M. Collins, R. Bluckis, P. A. J. Bagot, R. J. Harrison, Nanomagnetic properties of the meteorite cloudy zone. *Proc. Natl. Acad. Sci. U.S.A.* **115**, E11436–E11445 (2018).
25. M. Uehara, J. Gattacceca, H. Leroux, D. Jacob, C. J. van der Beek, Magnetic microstructures of metal grains in equilibrated ordinary chondrites and implications for paleomagnetism of meteorites. *Earth Planet. Sci. Lett.* **306**, 241–252 (2011).
26. A. Scholl, H. Ohldag, F. Nolting, J. Stöhr, H. A. Padmore, X-ray photoemission electron microscopy, a tool for the investigation of complex magnetic structures (invited). *Rev. Sci. Instrum.* **73**, 1362–1366 (2002).
27. R. J. Harrison, I. Lascu, FORCulator: A micromagnetic tool for simulating first-order reversal curve diagrams. *Geochem. Geophys. Geosyst.* **15**, 4671–4691 (2014).
28. C. Maurel, B. P. Weiss, J. F. J. Bryson, Meteorite cloudy zone formation as a quantitative indicator of paleomagnetic field intensities and cooling rates on planetesimals. *Earth Planet. Sci. Lett.* **513**, 166–175 (2019).
29. J. Yang, J. I. Goldstein, Magnetic contribution to the interdiffusion coefficients in bcc (α) and fcc (γ) Fe-Ni alloys. *Metall. Mater. Trans. A* **35**, 1681–1690 (2004).
30. W. S. Cassata, P. R. Renne, Systematic variations of argon diffusion in feldspars and implications for thermochronometry. *Geochim. Cosmochim. Acta* **112**, 251–287 (2013).
31. D. D. Bogard, D. H. Garrison, T. J. McCoy, Chronology and petrology of silicates from IIE iron meteorites: Evidence for a complex parent body evolution. *Geochim. Cosmochim. Acta* **64**, 2133–2154 (2000).
32. E. Dos Santos, J. Gattacceca, P. Rochette, G. Fillion, R. B. Scorzelli, Kinetics of tetrataenite disordering. *J. Magn. Magn. Mater.* **375**, 234–241 (2015).
33. H. Wang, B. P. Weiss, X.-N. Bai, B. G. Downey, J. Wang, J. Wang, C. Suavet, R. R. Fu, M. E. Zucolotto, Lifetime of the solar nebula constrained by meteorite paleomagnetism. *Science* **355**, 623–627 (2017).
34. R. Oran, B. P. Weiss, O. Cohen, Were chondrites magnetized by the early solar wind? *Earth Planet. Sci. Lett.* **492**, 222–231 (2018).
35. L. L. Hood, N. A. Artemieva, Antipodal effects of lunar basin-forming impacts: Initial 3D simulations and comparisons with observations. *Icarus* **193**, 485–502 (2008).
36. M. G. Sterenborg, J. W. Crowley, Thermal evolution of early solar system planetesimals and the possibility of sustained dynamos. *Phys. Earth Planet. Inter.* **214**, 53–73 (2013).
37. J. F. J. Bryson, J. A. Neufeld, F. Nimmo, Constraints on asteroid magnetic field evolution and the radii of meteorite parent bodies from thermal modelling. *Earth Planet. Sci. Lett.* **521**, 68–78 (2019).
38. F. Nimmo, Energetics of asteroid dynamos and the role of compositional convection. *Geophys. Res. Lett.* **36**, L10201 (2009).
39. H. J. Melosh, E. V. Ryan, E. Asphaug, Dynamic fragmentation in impacts: Hydrocode simulation of laboratory impacts. *J. Geophys. Res.* **97**, 14735–14759 (1992).
40. T. M. Davison, D. P. O'Brien, F. J. Ciesla, G. S. Collins, The early impact histories of meteorite parent bodies. *Meteorit. Planet. Sci.* **48**, 1894–1918 (2013).
41. W. F. Bottke Jr., D. D. Durda, D. Nesvorný, R. Jedicke, A. Morbidelli, D. Vokrouhlický, H. F. Levison, Linking the collisional history of the main asteroid belt to its dynamical excitation and depletion. *Icarus* **179**, 63–94 (2005).
42. W. F. Bottke, D. Vokrouchlicky, S. Marchi, T. Swindle, E. R. D. Scott, J. R. Weirich, H. Levison, Dating the Moon-forming impact event with asteroidal meteorites. *Science* **348**, 321–323 (2015).
43. S. M. Brown, L. T. Elkins-Tanton, Compositions of Mercury's earliest crust from magma ocean models. *Earth Planet. Sci. Lett.* **286**, 446–455 (2009).
44. S. N. Raymond, A. Izidoro, The empty primordial asteroid belt. *Sci. Adv.* **3**, e1701138 (2017).
45. W. F. Bottke, D. Nesvorný, R. E. Grimm, A. Morbidelli, D. P. O'Brien, Iron meteorites as remnants of planetesimals formed in the terrestrial planet region. *Nature* **439**, 821–824 (2006).

46. S. Fornasier, B. E. Clark, E. Dotto, A. Migliorini, M. Ockert-Bell, M. A. Barucci, Spectroscopic survey of M-type asteroids. *Icarus* **210**, 655–673 (2010).

47. L. T. Elkins-Tanton, E. Asphaug, J. F. Bell III, D. Bercovici, B. G. Bills, R. P. Binzel, W. F. Bottke, M. Brown, J. Goldsten, R. Jaumann, I. Jun, D. J. Lawrence, P. Lord, S. Marchi, T. Mc Coy, D. Oh, R. Park, P. N. Peplowski, C. A. Polanskey, D. Potter, T. H. Prettyman, C. A. Raymond, C. T. Russell, S. Scott, H. Stone, K. G. Sukhatme, N. Warner, B. P. Weiss, D. D. Wenkert, M. Wieczorek, D. Williams, M. T. Zuber, Asteroid (16) Psyche: Visiting a metal world, paper presented at the 48th Lunar Planetary Science Conference, The Woodlands, TX, 2017.

48. J. Stöhr, H. A. Padmore, S. Anders, T. Stammler, Principles of X-ray magnetic dichroism spectromicroscopy. *Surf. Rev. Lett.* **5**, 1297–1308 (1998).

49. N. Van Roosbroek, L. Pittarello, A. Greshake, V. Debaille, P. Claeys , First finding of impact melt in the IIE Netschaëvo meteorite. *Meteorit. Planet. Sci.* **51**, 372–389 (2016).

50. D. L. Cook, R. J. Walker, M. F. Horan, J. T. Wasson, J. W. Morgan, Pt-Re-Os systematics of group IIAB and IIIAB iron meteorites. *Geochim. Cosmochim. Acta* **68**, 1413–1431 (2004).

51. G. Wünnemann, G. S. Collins, H. J. Melosh, A strain-based porosity model for use in hydrocode simulations of impacts and implications for transient crater growth in porous targets. *Icarus* **180**, 514–527 (2006).

52. G. S. Collins, H. J. Melosh, B. A. Ivanov, Modeling damage and deformation in impact simulations. *Meteorit. Planet. Sci.* **39**, 217–231 (2004).

53. T. M. Davison, F. J. Ciesla, G. S. Collins, Post-impact thermal evolution of porous planetesimals. *Geochim. Cosmochim. Acta* **95**, 252–269 (2012).

54. T. S. Kruijer, T. Kleine, Age and origin of IIE iron meteorites inferred from Hf-W chronology. *Geochim. Cosmochim. Acta* **262**, 92–103 (2019).

55. R. J. Lyons, T. J. Bowling, F. J. Ciesla, T. M. Davison, G. S. Collins, The effects of impacts on the cooling rates of iron meteorites. *Meteorit. Planet. Sci.* **54**, 1604–1618 (2019).

56. A. M. Ruzicka, M. Hutson, Comparative petrology of silicates in the Udei Station (IAB) and Miles (IIE) iron meteorites: Implications for the origin of silicate-bearing irons. *Geochim. Cosmochim. Acta* **74**, 394–433 (2010).

57. H. Takeda, W. Hsu, G. R. Huss, Mineralogy of silicate inclusions of the Colomera IIE iron and crystallization of Cr-diopside and alkali feldspar from a partial melt. *Geochim. Cosmochim. Acta* **67**, 2269–2287 (2003).

58. A. M. Ruzicka, G. W. Fowler, G. A. Snyder, M. Prinz, J. J. Papike, L. A. Taylor, Petrogenesis of silicate inclusions in the Weekeroo Station IIE iron meteorite: Differentiation, remelting, and dynamic mixing. *Geochim. Cosmochim. Acta* **63**, 2123–2143 (1999).

59. J. I. Goldstein, E. R. D. Scott, N. L. Chabot, Iron meteorites: Crystallization, thermal history, parent bodies, and origin. *Geochemistry* **69**, 293–325 (2009).

60. D. J. Dunlop, Ö. Özdemir, *Rock Magnetism: Fundamentals and Frontiers* (Cambridge Univ. Press, 1997), pp. 1–573.

61. J. F. J. Bryson, J. Herrero-Albillos, F. Kronast, M. Ghidini, S. A. T. Redfern, G. van der Laan, R. J. Harrison, Nanopaleomagnetism of meteoritic Fe-Ni studied using X-ray photoemission electron microscopy. *Earth Planet. Sci. Lett.* **396**, 125–133 (2014).

62. G. S. Watson, A test for randomness of directions. *Geophys. J. Int.* **7**, 160–161 (1956).

63. G. S. Watson, Large sample theory of the Langevin distribution. *J. Stat. Plan. Infer.* **8**, 245–256 (1983).

64. N. I. Fisher, T. Lewis, B. J. J. Embleton, *Statistical Analysis of Spherical Data* (Cambridge Univ. Press 1987), chap. 5.

65. T. Berndt, A. R. Muxworthy, K. Fabian, Does size matter? Statistical limits of paleomagnetic field reconstruction from small rock specimens. *J. Geophys. Res.* **121**, 15–26 (2016).

66. S. Yeem, R. J. Harrison, Interaction-driven domain-state transition in the meteorite cloudy zone: A hybrid micromagnetic approach to modelling remanence acquisition, paper presented at the AGU Fall Meeting, San Francisco, CA, 2019.

67. J. F. J. Bryson, C. I. O. Nichols, J. Herrero-Albillos, F. Kronast, T. Kasama, H. Alimadadi, G. van der Laan, F. Nimmo, R. J. Harrison, Long-lived magnetism from solidification-driven convection on the pallasite parent body. *Nature* **517**, 472–475 (2015).

68. J. F. J. Bryson, B. P. Weiss, R. J. Harrison, J. Herrero-Albillos, F. Kronast, Paleomagnetic evidence for dynamo activity driven by inward crystallisation of a metallic asteroid. *Earth Planet. Sci. Lett.* **472**, 152–163 (2017).

69. C. I. O. Nichols, J. F. J. Bryson, R. Blukis, J. Herrero-Albillos, F. Kronast, R. Rüffer, A. I. Chumakov, R. J. Harrison, Variations in the magnetic properties of meteoritic cloudy zone. *Geochem. Geophys. Geosyst.* **21**, e2019GC008798 (2020).

70. M. Terho, L. J. Pesonen, I. T. Kukkonen, *The Petrophysical Classification of Meteorites: New Results* (Report Q29.1/91/1, Geological Survey of Finland, 1993), pp. 1–68.

71. N. S. Bezaeva, J. Gattacceca, P. Rochette, R. A. Sadykov, V. I. Trukhin, Demagnetization of terrestrial and extraterrestrial rocks under hydrostatic pressure up to 1.2 GPa. *Phys. Earth Planet. Inter.* **179**, 7–20 (2010).

72. J. Schindelin, I. Arganda-Carreras, E. Frise, V. Kaynig, M. Longair, T. Pietzsch, S. Preibisch, C. Rueden, S. Saalfeld, B. Schmid, J.-Y. Tinevez, D. J. White, V. Hartenstein, K. Eliceiri, P. Tomancak, A. Cardona, Fiji: An open-source platform for biological-image analysis. *Nat. Methods* **9**, 676–682 (2012).

73. E. R. D. Scott, J. I. Goldstein, Thermal histories and origins of group IIE and IAB iron meteorites and their parent asteroids, paper presented at the 47th Lunar and Planetary Science Conference, The Woodlands, TX, 2016.

74. D. Porter, K. Easterling, M. Sherif, *Phase Transformations in Metals and Alloys* (CRC Press, ed. 3, 2004), chap. 5.

75. U. R. Christensen, V. Holzwarth, A. Reiners, Energy flux determines magnetic field strength of planets and stars. *Nature* **457**, 167–169 (2009).

76. J. Gattacceca, P. Rochette, Toward a robust normalized magnetic paleointensity method applied to meteorites. *Earth Planet. Sci. Lett.* **227**, 377–393 (2004).

77. E. R. D. Scott, T. V. Krot, J. I. Goldstein, S. Wakita, Thermal and impact history of the H chondrite parent body during metamorphism: Constraints from metallic Fe–Ni. *Geochim. Cosmochim. Acta* **136**, 13–37 (2014).

78. J. Gattacceca, C. Suavet, P. Rochette, B. P. Weiss, M. Winklhofer, M. Uehara, J. M. Friedrich, Metal phases in ordinary chondrites: Magnetic hysteresis properties and implications for thermal history. *Meteorit. Planet. Sci.* **49**, 652–676 (2014).

79. C. I. O. Nichols, J. F. J. Bryson, J. Herreros-Albillos, F. Konrast, F. Nimmo, R. J. Harrison, Pallasite paleomagnetism: Quiescence of a core dynamo. *Earth Planet. Sci. Lett.* **441**, 103–112 (2016).

80. E. M. Shoemaker, Interpretation of lunar craters, in *Physics and Astronomy of the Moon*, Z. Kopal, Ed. (Academic Press, 1961), pp. 283–359.

81. T. M. Davison, F. J. Ciesla, G. S. Collins, D. Elbeshausen, The effect of impact obliquity on shock heating in planetesimal collisions. *Meteorit. Planet. Sci.* **49**, 2252–2265 (2014).

82. K. A. Holsapple, The scaling of impact processes in planetary sciences. *Annu. Rev. Earth Planet. Sci.* **21**, 333–373 (1993).

83. T. S. Kruijer, C. Burkhardt, G. Budde, T. Kleine, Age of Jupiter inferred from the distinct genetics and formation times of meteorites. *Proc. Natl. Acad. Sci. U.S.A.* **114**, 6712–6716 (2017).

84. W. F. Bottke Jr., D. D. Durda, D. Nesvorny, R. Jedicke, A. Morbidelli, D. Vokrouhlicky, H. Levison, The fossilized size distribution of the main asteroid belt. *Icarus* **175**, 111–140 (2005).

85. W. F. Bottke Jr., M. C. Nolan, R. Greenberg, R. A. Kolvoord, Velocity distributions among colliding asteroids. *Icarus* **107**, 255–268 (1994).

86. E. Asphaug, C. B. Agnor, Q. Williams, Hit-and-run planetary collisions. *Nature* **439**, 155–160 (2006).

87. A. Emsenhuber, E. Asphaug, Fate of the runner in hit-and-run collisions. *Astrophys. J.* **875**, 95 (2019).

Science Advances

Meteorite evidence for partial differentiation and protracted accretion of planetesimals

Clara Maurel, James F. J. Bryson, Richard J. Lyons, Matthew R. Ball, Rajesh V. Chopdekar, Andreas Scholl, Fred J. Ciesla, William F. Bottke and Benjamin P. Weiss

ARTICLE TOOLS	http://advances.sciencemag.org/content/6/30/eaba1303
SUPPLEMENTARY MATERIALS	http://advances.sciencemag.org/content/suppl/2020/07/20/6.30.eaba1303.DC1
REFERENCES	This article cites 77 articles, 9 of which you can access for free http://advances.sciencemag.org/content/6/30/eaba1303#BIBL
PERMISSIONS	http://www.sciencemag.org/help/reprints-and-permissions

Use of this article is subject to the Terms of Service